Available online at www.sciencedirect.com

ScienceDirect

Procedia Structural Integrity 2 (2016) 911–918

Structural Integrity Procedia

www.elsevier.com/locate/procedia

21st European Conference on Fracture, ECF21, 20-24 June 2016, Catania, Italy

# Experimental and simulated displacement in cracked specimen of P91 steel under creep conditions

F. Bassi[a,*] , A. Saxena[b], A. Lo Conte[a], S. Beretta[a], M. E. Cristea[c]

[a]*Politecnico di Milano, Milano 20156, Italy*
[b]*University of Arkansas, Fayetteville AR 72701, USA*
[c] *Tenaris, Dalmine 24040, Italy*

**Abstract**

The assessment of crack initiation and propagation under creep conditions is important in the remaining life prediction of pipe components for power generation industry. One of the most successful analytical parameters for describing crack propagation under steady-state creep conditions is the C*-Integral that depends strongly on the material's creep behavior and the resulting load-line displacement. This study deals with the determination and optimization of a creep model for a P91 grade steel operating at 600 °C. After a good fit provided by the model with uniaxial creep tests was found, the creep behavior of compact type C(T) specimens was modeled to predict creep crack growth (CCG) rates. A modified Cocks and Ashby power law creep controlled cavity growth model was used to compute the creep crack propagation rates. Load-line deflection was found to be strongly dependent on the primary creep strain rate. Lastly, good correlation between the experimental CCG results and the predicted CCG rates from the simulations were found.


Peer-review under responsibility of the Scientific Committee of ECF21.

*Keywords:* Creep damage, Creep crack growth, Finite element damage analysis

## 1. Introduction

The numerical prediction of reliable creep crack initiation and growth data is extremely important in the residual life assessment of power plant components operating at high temperatures that contain pre-existing or service generated defects. Predicting the CCG behavior typically depends on two models:

- uniaxial creep deformation models that explicitly admit cavitation damage, and
- models that extend the uniaxial creep behavior to the multiaxial stress state that is present at the tips of cracks.


Peer-review under responsibility of the Scientific Committee of ECF21.
10.1016/j.prostr.2016.06.117

The first set of models can be further divided into two groups, time and strain dependent respectively, according to the state variable that is used to describe the creep strain rate. Among the time dependent models, the one by Kachanov (1958) uses a continuum damage mechanics approach to predict creep strain in both uniaxial and multiaxial conditions. Much later, Liu and Murakami (1998), introduced a new approach by defining creep damage based micromechanics which also can be expressed in a multiaxial form. Thus, both can be directly used to predict creep crack growth in cracked components. In the context of strain dependent models, Graham and Walles (1955) proposed an approach based on the summation of three power laws to describe primary secondary and tertiary uniaxial creep behavior. This method also accounts for temperature dependence which, for the purpose of this paper, has not been utilized because the tests for verifying the models were all conducted at a single temperature. A difference between this and the previous models is that this model does not consider a damage variable in the creep strain rate definition. Its non-explicit time dependence through strain leads to fewer numerical issues during finite element simulations related to time integration. However, the Graham-Walles model cannot be directly used to simulate creep crack propagation but it can be combined with other approaches such as one that utilize ductility exhaustion under multiaxial stress states. The method by Cocks and Ashby (1980) is ideal for this purpose since it is able to predict intergranular fracture during power-law creep expressing the ratio between multiaxial and uniaxial creep ductility based on the stress triaxiality and the Norton's law creep exponent, $n$. This model was modified by Wen and Tu (2014) to improve the multiaxial creep ductility dependence on stress triaxiality. Section 2 of the paper shows the material properties and the experimental data of the modified grade 91 steel that were used to determine the material constants of the Graham-Walles uniaxial creep model. Section 3 summarizes the finite element procedures that were used first to validate the Graham-Walles fit on round specimens and then to perform 2D and 3D simulations on compact type C(T) specimens to predict the onset of creep crack growth and the subsequent creep crack growth rates. The results of numerical simulations are compared with the experimental data in Section 4. From these results, the crack propagation parameter for steady-state creep was calculated and compared. Finally, this paper ends with the conclusions in Section 5.

**Nomenclature**

| | |
|---|---|
| $a_0$ | initial crack length |
| $A, n$ | Norton law coefficients |
| $A_i, n_i, m_i$ | Graham-Walles model coefficients |
| $B, B_n$ | CCG specimen thickness and net thickness |
| $C^*$ | $C^*$ parameter for steady state creep |
| $(da/dt)$ | crack propagation rate |
| $E$ | Young's modulus |
| $(F^I/F)$ | C(T) specimen shape function derivative normalized on the shape function |
| $K_0$ | initial stress intensity factor |
| $LLD$ | load-line displacement |
| $P$ | applied load |
| $t_f$ | failure time |
| $t_T$ | transient time |
| $W$ | CCG specimen width |
| $\Delta a, \Delta a_f$ | crack and final crack extension |
| $\Delta t$ | time increment of the numerical simulations |
| $\dot{\Delta}_c$ | load-line displacement creep rate |
| $\varepsilon_f, \varepsilon_f^*$ | uniaxial and multiaxial creep ductility |
| $\varepsilon_{true}$ | true strain in tensile tests |
| $\dot{\varepsilon}_{ss}, \dot{\varepsilon}_c, \varepsilon_c$ | steady state creep strain rate, creep strain rate and creep strain |
| $\omega, \dot{\omega}$ | damage and damage rate |
| $\sigma, \sigma_h, \sigma_{eq}$ | nominal, hydrostatic and equivalent stress |
| $\sigma_{true}$ | true stress in tensile tests |

## 2. Material properties and experimental tests

The material analyzed in this study is a modified grade 91 steel that is designed to operate at 600 °C. All the experimental tests contained in this section have been performed on specimens extracted directly from a pipe. The elastic properties reported in Fig. 1 a) have been extracted from the shown stress-strain data taken from a high temperature tensile test performed on cylindrical specimens.

Uniaxial creep tests were performed at 600 °C at different stress levels between 90 MPa and 160 MPa also using cylindrical specimens designed according to the ASTM E139-11 (2011) standard with a diameter of 10 mm and a gage length of 50 mm. The results from these tests show in Fig. 3 a rupture time range between 600 h and 100000 h in full agreement with the grade 91 steel data contained in API 579-1 (2007). The steady state creep strain rate $\dot{\varepsilon}_{ss}$ as a function of the stress $\sigma$ was fitted to the Norton's power-law $\dot{\varepsilon}_{ss} = A\,\sigma^{n}$. The data shown in Fig. 1 b) exhibit a change in the trend at a stress level $\sigma$ of 112 MPa. For this reason, two sets of $A$ and $n$ material constants at low and high stresses are determined from regression of the data.

Creep crack growth tests were performed at 600 °C on the geometry shown in Fig. 2 as per ASTM E1457-13 (2013) standard. Side grooves reduced the section thickness $B$ to the net section thickness $B_n$ in order to achieve a straighter crack front. Crack propagation was monitored through the potential drop (PD) measurement system (Belloni et al. (2002)) and the test temperature of 600 °C was controlled to allow a fluctuation of no more than $\pm 1$ °C. Test conditions are fully described in Table 1.

Table 1. CCG test data of P91 at 600 °C.

| $W$ (mm) | $B$ (mm) | $B_n$ (mm) | $a_0$ (mm) | $K_0$ $(MPa\,m^{0.5})$ | $P$ (N) | $\Delta a_f$ (mm) |
|---|---|---|---|---|---|---|
| | | | 12.30 | 15.0 | 2940 | 2.4 |
| 25.4 | 12.7 | 10.1 | 12.32 | 19.6 | 3825 | 1.8 |
| | | | 12.32 | 21.8 | 4270 | 2.7 |

## 3. Numerical simulation models

Among the creep models introduced in Section 1, the Graham-Walles was chosen to represent the uniaxial creep behaviour for the grade 91 steel. The simplified Graham-Walles creep model of Eq. (1), consists in the superposition of three power-laws to determine creep strain rate $\dot{\varepsilon}_c$ in primary, secondary and tertiary creep conditions depending on the stress level $\sigma$ and the creep strain $\varepsilon_c$.

$$\dot{\varepsilon}_c = A_1\sigma^{n_1}\varepsilon_c^{m_1} + A_2\sigma^{n_2}\varepsilon_c^{m_2} + A_3\sigma^{n_3}\varepsilon_c^{m_3} \tag{1}$$

It is worth noting that this model does not explicitly have time as a parameter and is therefore different in that respect from the Kachanov and Liu-Murakami models. Since the creep strain is a function of time, the time is implicit in the model. As a consequence, the finite element simulations are less affected by the numerical integration steps that are expressed in terms of changes in creep strain instead of time. The Graham-Walles creep model was fitted to the creep data in Fig. 3 in order to determine the 9 material constants $A_i, n_i$ and $m_i$ listed in Table 2 through the least squares regression method.

Table 2. Graham-Walles material constants of P91 at 600 °C. All $A_i$ constants are expressed in $(h^{-1}MPa^{-n})$

| $A_1$ | $A_2$ | $A_3$ | $n_1$ | $n_2$ | $n_3$ | $m_1$ | $m_2$ | $m_3$ |
|---|---|---|---|---|---|---|---|---|
| 2.2202E-42 | 7.7542E-12 | 4.1497E-13 | 16.421 | 1.4499 | 6.0325 | -0.7133 | -0.8041 | 3.6898 |

The commercial finite element software *ABAQUS* and its user subroutines were used for all the numerical simulations contained in this work. A 3D axisymmetric model of the creep specimen was created to validate the material constants of the Graham-Walles model. Because of symmetry only a quarter of the specimen was analyzed with the appropriate constraint conditions. Four node axisymmetric elements were used with an element size of 100 $\mu m$ close to the midline section where diameter was reduced by 0.1 mm to localize creep strain in this area. The *CREEP* user subroutine was written according to Eq. (1) in order to predict the creep behavior at different stress levels between 90 MPa and 160

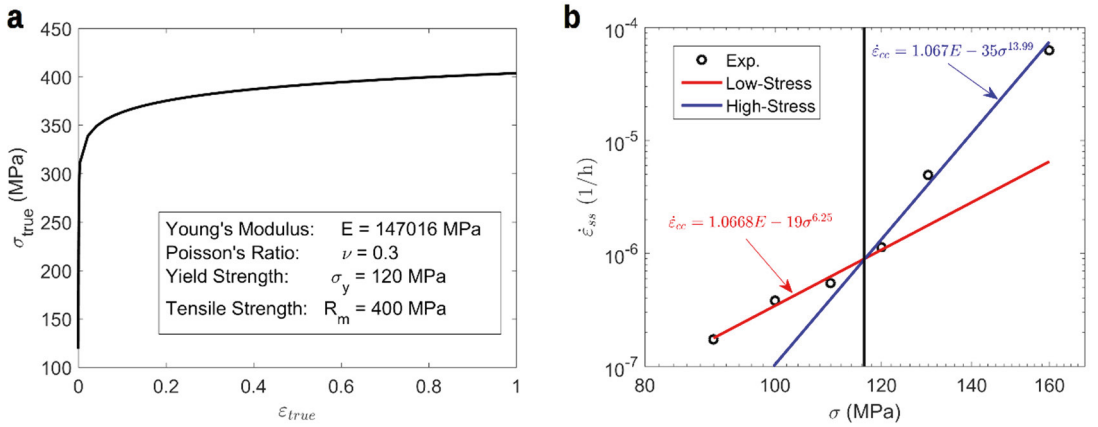


Fig. 1. Tensile and creep properties of P91 at 600 °C: a) Uniaxial stress-strain data of P91 at 600°C b) Norton law fit of the steady state creep strain rate as a function of applied stress.

MPa. The results are plotted in Fig. 3 and show a good agreement with the experimental data. It might be noted that the prediction at 130 MPa overestimates the failure time whereas at all other stress levels the failure time is under-predicted. This is partially due to data scatter that is normally observed in such testing as also noted by Walles and Graham (1961). The creep strain rate of the numerical simulations is shown as a function of time and compared with the experimental data in Fig. 4. The primary creep phase is well represented and is expected to be important in the load-line displacement evaluations for the CCG simulations using compact type test specimens.

Creep crack growth was modeled with a ductility exhaustion approach that defines the damage rate $\dot{\omega}$ as the ratio between the creep strain rate $\dot{\varepsilon}_c$ and the multiaxial creep ductility $\varepsilon_f$ according to Eq. (2)

$$\dot{\omega} = \frac{\dot{\varepsilon}_c}{\varepsilon_f^*} \quad \rightarrow \quad \omega_i = \omega_{i-1} + \dot{\omega}_i \Delta t \tag{2}$$

where, $\Delta t$ is the time increment in the simulations. Multiaxial creep ductility can be expressed by the Cocks and Ashby (1980) grain-boundary cavity growth theory. This model is based on the definition of the creep ductility ratio under multiaxial and uniaxial conditions $\left(\varepsilon_f^*/\varepsilon_f\right)_{C-A}$ given by Eq. (3)

$$\left(\frac{\varepsilon_f^*}{\varepsilon_f}\right)_{C-A} = \sinh\left[\frac{2}{3}\left(\frac{n-0.5}{n+0.5}\right)\right] \Big/ \sinh\left[2\left(\frac{n-0.5}{n+0.5}\right)\frac{\sigma_h}{\sigma_{eq}}\right] \tag{3}$$

where $\sigma_h$ and $\sigma_{eq}$ are the hydrostatic and the equivalent stress components respectively. The multiaxial ductility therefore depends on the stress triaxiality that is present at the crack tip and the Norton law exponent $n$ which, for the following finite element simulations, was chosen equal to 10, i.e. an intermediate value between the low and high stresses constants of Fig. 1 b). As previously discussed, Wen and Tu (2014) proposed a modification of Eq. (3) by changing the equation that fits creep ductility as shown in Eq. (4):

$$\left(\frac{\varepsilon_f^*}{\varepsilon_f}\right)_{W-T} = \exp\left[\frac{2}{3}\left(\frac{n-0.5}{n+0.5}\right)\right] \Big/ \exp\left[2\left(\frac{n-0.5}{n+0.5}\right)\frac{\sigma_h}{\sigma_{eq}}\right] \tag{4}$$

This multiaxial ductility expression was used to estimate CCG in the finite element models of Fig. 5. Because of the scatter in the experimental data, different values of uniaxial creep ductility $\varepsilon_f$ were chosen for a sensitivity study in both 2D and 3D simulations. The elastic-plastic properties of Section 2 were applied to both models while the creep behavior was described by the *CREEP* user subroutine previously discussed. The element size close to the crack tip was kept equal to 100 $\mu m$ which is on the order of the grain size.

Considering the symmetry, in the 2D model only half of the C(T) specimen was analyzed. Because of the limitations of this model, side grooves were not considered. Crack propagation was obtained by applying a multi-

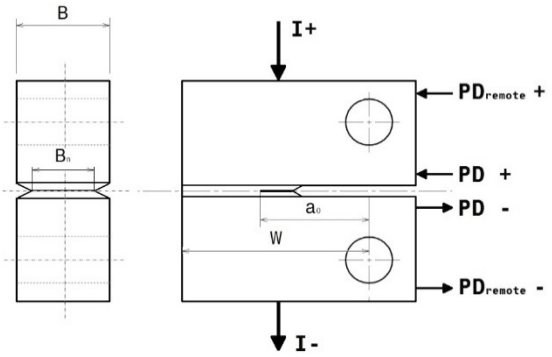


Fig. 2. Schematic representation of a CCG specimen and the potential drop method.

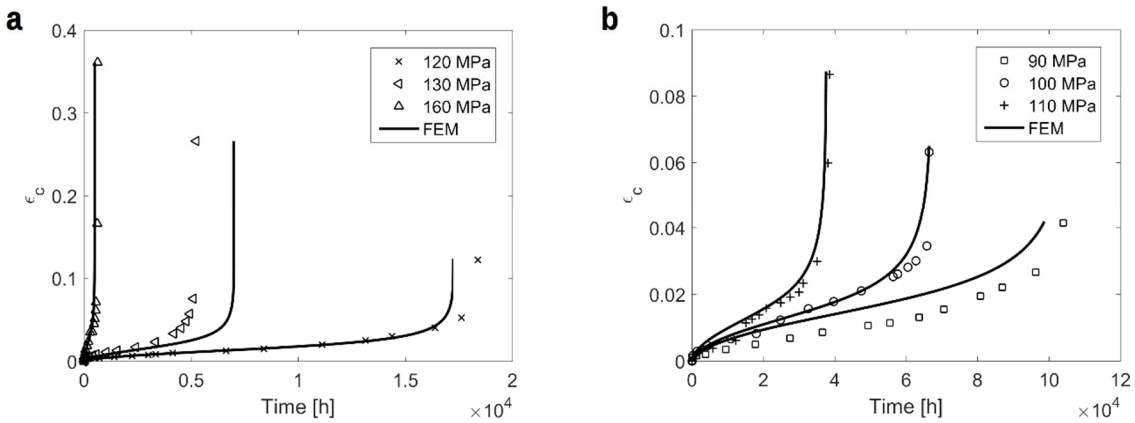


Fig. 3. Comparison of finite element simulations with experimental uniaxial creep data: a) high stress levels (b) low stress levels.

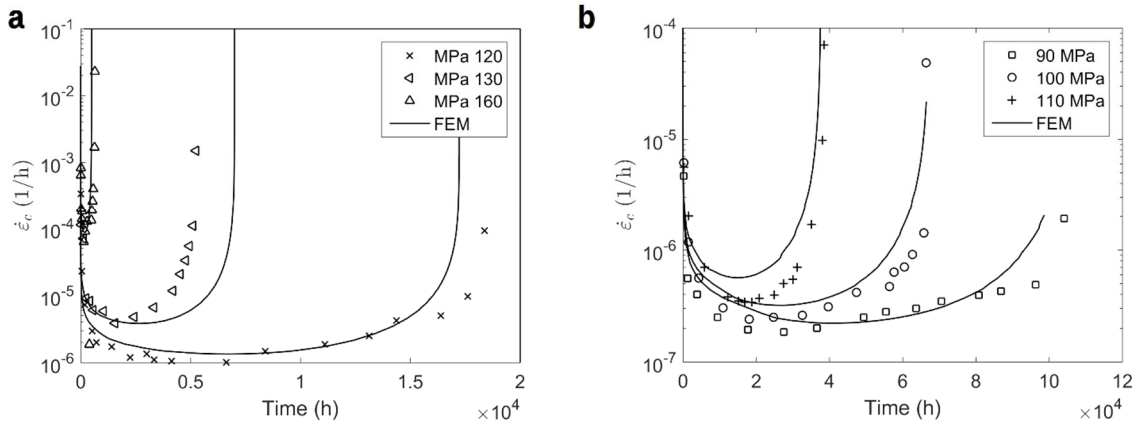


Fig. 4. Creep strain rate as a function of time for the finite element simulations and comparison with experimental uniaxial creep data: a) high stress levels b) low stress levels.

point constraint to the red section of Fig. 6 a). A *MPC* user subroutine was defined in order to release the element at the crack tip as soon as both its integration points that lie on the ligament surface reach a damage value greater or equal 0.99. Four nodes plane strain elements with full integration were used.

Because of the symmetry, in the 3D model only a quarter of the specimen was analyzed. The crack propagation is

controlled by a field variable defined in the *USDFLD* user subroutine so that as soon as the damage reaches a value of 0.99, the elastic modulus $E$ is gradually reduced to a unit value. With a low elastic modulus, the element is no longer able to support stresses simulating crack propagation conditions. In this simulation side grooves were considered in order to obtain a realistic representation of the actual specimen that was used in the experimental CCG tests. For this purpose, eight nodes hexahedral elements with reduced integration were used (Fig. 6 b).

## 4. Results and comparison with the experimental tests

All the finite element simulations were performed until the failure time of the experimental test was reached while the same time steps of the uniaxial creep simulations were applied. Results in terms of load-line displacement and crack propagation as a function of normalized time and comparison with the experimental data are shown in Fig. 8. The optimum value of uniaxial ductility $\varepsilon_f$ used in the simulations was found to be equal to 0.13 and 0.24 for 2-dimensional and 3-dimensional simulations respectively. These values are consistent with the creep rupture data of Fig. 3 based on elongation ($0.04 \leq \varepsilon_f \leq 0.36$). Although crack propagation is predicted very well for all initial stress intensity factors, the simulated load-line displacement gives a good correlation with the corresponding experimental results at $K_0 = 15\ MPa\ m^{0.5}$. This might be an indication that the uniaxial creep behavior is accurately represented at low stresses while at higher stresses additional uniaxial creep tests are required. In fact in Fig. 8 a), the main difference with the experimental data is in the primary part of the curve which strongly depends on creep behavior, while in the second and third part of the curve that depends on crack propagation, the load-line displacement slope is consistent with the simulated values. A sensitivity analysis of the numerical simulations with respect to the uniaxial ductility is shown in Fig. 7 a) and b) where the optimum values of $\varepsilon_f$ of 0.13 and 0.24 have been applied to both models. The 3-dimensional model is significantly affected by the uniaxial creep ductility variation in terms of load-line displacement and crack propagation compared with the 2-dimensional model. The time to failure of the *C(T)* specimen is reduced to approximately 1/10 of the experimental value. Since creep ductility $\varepsilon_f$ of 0.24 is closer to the creep ductility data at high stresses in Fig. 3, it is expected to represent the crack tip conditions better. The lower value of $\varepsilon_f$ found for the 2D model, suggests that the studied specimen represents an intermediate situation between plane stress and plane

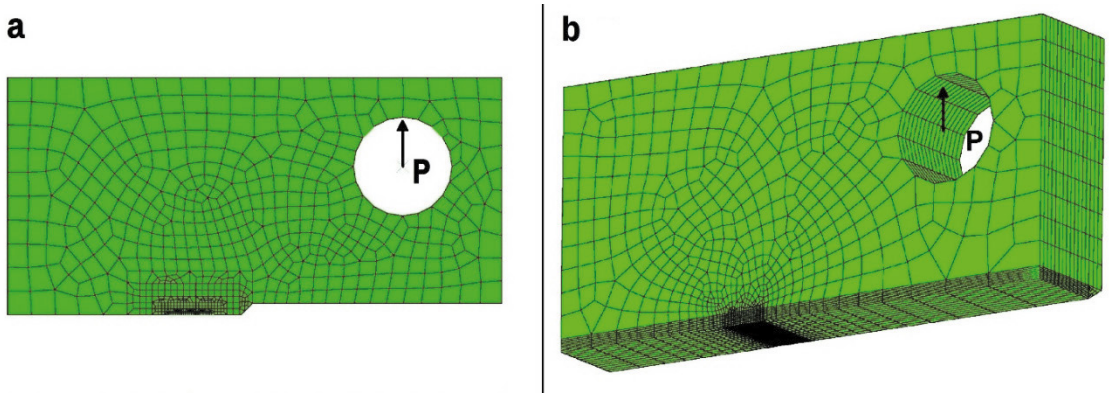


Fig. 5. Schematic representation of the finite element models: a) 2D b) 3D.

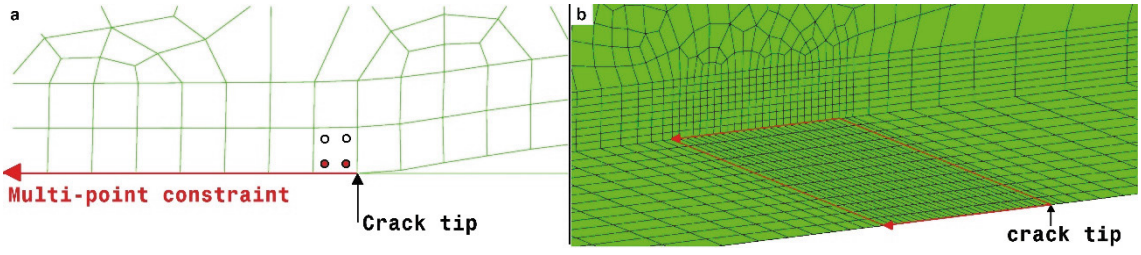


Fig. 6. Finite element simulations: crack front detail of 2D model a) and 3D models b).

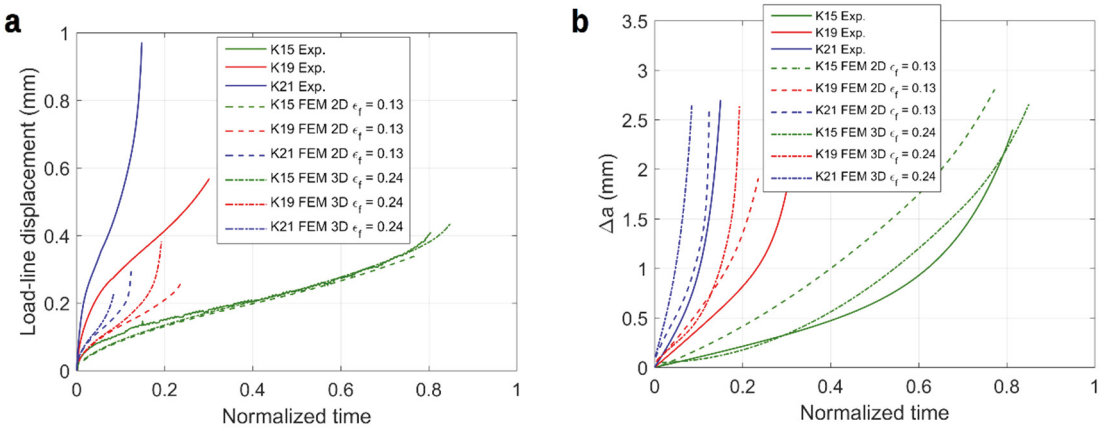


Fig. 8. Finite element simulation results and comparison with the experimental CCG data: a) load-line displacement b) crack propagation.

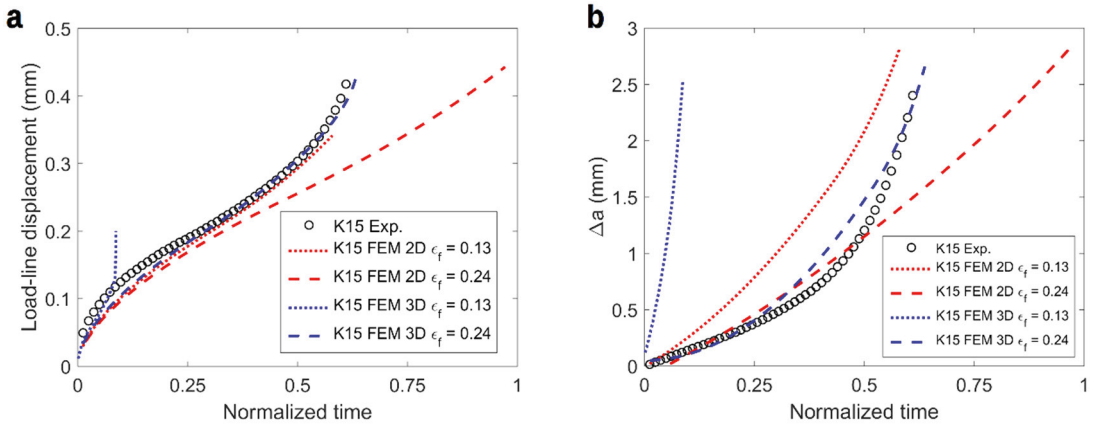


Fig. 7. Numerical simulations sensitivity to uniaxial creep ductility. a) load-line displacement b) crack propagation.

strain conditions. Therefore a lower uniaxial ductility is needed in order to avoid overestimating the experimental failure time. Although in both models the crack growth rates are very sensitive to uniaxial creep ductility which does imply that if the creep ductility varies we can expect large variations in the creep crack growth rates.

From the crack propagation and the load line displacement results of the simulation at $K_0 = 15\ MPa\ m^{0.5}$, it was possible to estimate the crack tip parameter $C^*$ for steady state creep condition and compare it with the *C(t)* integral values calculated by the finite element software *ABAQUS*. The $C^*$ parameter was calculated according to Eq. (5) (Saxena (1980)) for the numerical simulations as well as the experimental data

$$C^* = \frac{P\dot{\Delta}_c}{B_n(W-a)}\left[2 + .522\left(1 - \frac{a}{W}\right)\right]\frac{n}{n+1} \tag{5}$$

where $\dot{\Delta}_c$ is the load line displacement rate associated to the creep deformation. Fig. 9 a) shows the crack propagation rate $(da/dt)$ as a function of the normalized $C^*$ for the numerical simulations, the experimental results and the comparison with the *C(t)* integral calculated using a large contour as the path surrounding the entire ligament. All the data in Fig. 9 are plotted starting from the transient time $t_T$ of 35 hours calculated as per definition by ASTM E1457-13 standard. The transient time was also verified through the finite element analysis by evaluating the $C(t)$ integral at two different contours, one small close to the crack tip that was automatically updated at every node release and the other significantly larger in order to encompass the entire ligament. The two contour integrals trend to a unique value after 30 hours of simulation demonstrating the path independence of $C(t)$ thus indicating that the steady state creep conditions are reached quickly under these test conditions. A significant similarity was found between the

experimental data and the 3D simulations at large crack sizes leading to the similar final crack front shown in Fig. 9 b). On the other hand, the 2D-simulation shows considerable differences in the calculated $C^*$ and the numerical $C(t)$ integral. However, numerical simulations and experimental data suggest that the relationship between crack propagation rate $(da/dt)$ and $C^*$ is not unique as seen in both experiments and simulations.

## 5. Conclusions

In this paper the combination of a uniaxial creep model and a ductility exhaustion approach was used to predict creep crack initiation and growth in C(T) specimens. The simplified model by Graham-Walles, was fitted to uniaxial creep experimental data at 600 °C of a modified grade 91 steel in order to predict the material's behavior at high temperature. A ductility exhaustion approach was used to estimate creep damage in cracked specimens by using the multiaxial ductility calculated with the Wen and Tu model based on the void growth theory by Cocks and Ashby. These models were integrated in a finite element software in order to perform 2D and 3D numerical assessments of crack propagation and load-line displacement at different load conditions. The results show a good agreement with the experimental data in terms of crack propagation. However at higher stresses the load-line displacement is slightly underestimated. A sensitivity analysis on the uniaxial creep ductility $\varepsilon_f$ showed a large dependence for the 3D model and less for the 2D model. Finally, the crack propagation parameter $C^*$ for steady state creep was calculated for the simulations and the experimental data and compared with the *C(t)* integral numerically evaluated by the finite element software on a crack contour. The 3D model showed a good correlation not only with the calculated *C(t)* integral but also with the experimental data in particular at higher crack propagation rates.

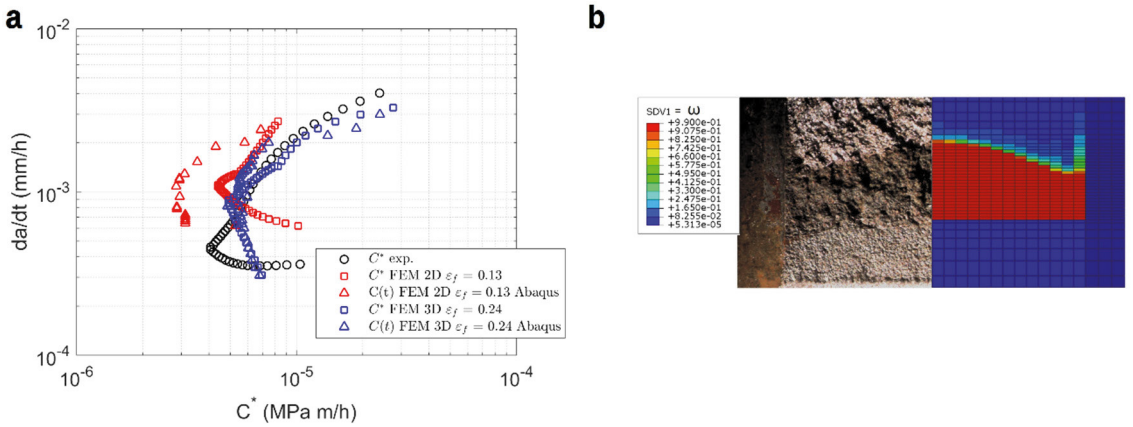


Fig. 9. Finite element simulation results and comparison with the experimental CCG data:
a) crack propagation as a function of the normalized $C^*$ parameter and $C(t)$ integral numerically calculated
b) experimental and numerical final crack front of the 3D simulation.

## References

Kachanov L. M., 1958. Time to the Fracture Process under Creep Conditions. Izv. Akad. SSSR OTN Teckh. Nauk, 8, 26.

Liu, Y., Murakami, S., 1998. Damage Localization of Conventional Creep Damage Models and Propositioins of a New Model for Creep Damage Analysis. JSME International Journal Series A 41(1), 57-65.

Graham, A., Walles, K. F. A., 1955. Relationship between Long- and Short-Time Creep and Tensile Properties of a Commercial Alloy. Journal of the Iron and Steel Institute 179, 104-121.

Cocks, A. C. F., Ashby, M. F., 1980. Intergranular fracture during power-law creep under multiaxial stresses. Metal Sci., 395-402.

Wen, Jian-Feng and Tu, Shan-Tung, 2014. A multiaxial creep-damage model for creep crack growth considering cavity growth and microcrack interaction. Engineering Fracture Mechanics 123, 197-210.

ASTM E139-11, 2011. Standard Test Methods for Conducting Creep, Creep-Rupture and Stress-Rupture Tests of Metallic Materials. ASTM.

API 579-1/ASME FFS-1, 2007. The American Society of Mechanical Engineers, 2007. Fitness-For-Service, June 5.

ASTM E1457-13, 2013. Standard Test Method for Measurement of Creep Crack Growth Times and Rates in Metals. ASTM.

Belloni, G., Gariboldi, E., Lo Conte, A., Tono, M., Speranzoso, P., 2002. On the experimental calibration of potential drop system for crack length of compact tension specimen measurements. Journal of Testing and Evaluation 30, 461-469.

Walles, K. F. A., Graham, A., 1961. On the Extrapolation and Scatter of Creep Data. A.R.C. C.P. No. 680.

Saxena, A., 1980. Evaluation of C* for the Characterization of Creep Crack Growth Behavior in 304 Stainless Steel. Fracture Mechanics: Twelth Conference, ASTM STP 700, ASTM, 131-151.